

Gas temperature and electron density profiles in an argon dc microdischarge measured by optical emission spectroscopy

Sergey G. Belostotskiy,^{1,a)} Tola Ouk,¹ Vincent M. Donnelly,^{1,a)} Demetre J. Economou,^{1,a)} and Nader Sadeghi^{2,b)}

¹Department of Chemical and Biomolecular Engineering, Plasma Processing Laboratory, University of Houston, Houston, Texas 77204-4004, USA

²Laboratoire de Spectrométrie Physique (UMR C5588), Université J. Fourier de Grenoble & CNRS, BP 87, F38402, Saint Martin d'Hères CedexFrance

(Received 3 December 2009; accepted 18 January 2010; published online 5 March 2010)

Optical emission spectroscopy was employed to study a high pressure (100 s of Torr), slot-type (600 μm interelectrode gap), argon dc microdischarge, with added traces of nitrogen. Spatially resolved gas temperature profiles were obtained by analyzing rovibrational bands of the N_2 first positive system. The gas temperature peaked near the cathode and increased with current. The contribution of Stark broadening to the hydrogen H_β emission lineshape was used to extract the electron density. The axial distribution of electron density as well as visual observation revealed that the microdischarge positive column was highly constricted. The electron density near the sheath edge increased with both pressure and current. © 2010 American Institute of Physics.

[doi:10.1063/1.3318498]

I. INTRODUCTION

High pressure (100 s of Torr) nonequilibrium microdischarges are the subject of considerable research due to their widespread applications or potential applications in plasma display panels, excimer radiation sources, sensors, materials treatment and modification, sterilization, plasma surgery, etc.^{1–18}

Plasma diagnostics are important to better understand microdischarge physics, which in turn, may be used for improved device performance. Optical emission spectroscopy (OES) is a well-established, nonintrusive diagnostic that is relatively easy to implement, despite the small dimensions of microdischarges.^{9,11,16,19,20} However, the information obtained by OES is often indirect. Thus, any assumptions made to aid in data interpretation must be carefully scrutinized.

In previous studies, laser Thomson scattering (LTS) and diode laser absorption spectroscopy were employed to measure electron density and electron temperature,¹⁴ as well as argon metastable ($1s_5$) density and gas temperature,¹⁸ in a slot-type dc argon microdischarge. In the present work, spatially resolved measurements of gas temperature and electron density were performed using trace gas (nitrogen and hydrogen) OES. The gas temperature (T_g) was extracted by analyzing the rovibrational band of the N_2 first positive system, while the electron density was deduced from the contribution of Stark broadening to the hydrogen H_β emission lineshape.

II. EXPERIMENTAL APPARATUS

The schematic of the experimental setup is presented in Fig. 1. A slot-type microdischarge^{9,12} was sustained between

two molybdenum electrodes, spaced 600 μm apart. The dimensions of the rectangular electrode surfaces facing the discharge were $5 \times 0.5 \text{ mm}^2$.

Plasma emission was imaged with an $f=30 \text{ mm}$ focal length achromatic lens ($7\times$ magnification) on the entrance slit (100 μm width) of each of two monochromators: (i) a high resolution 2 m focal length monochromator (Sopra SA), equipped with a 1200 groves/mm grating working in the third diffraction order, that was used to record the lineshape of H_β , Ar, and Ar^+ emissions and (ii) a 1 m focal length monochromator (Jobin-Yvon, HR1000), equipped with a 1200 groves/mm grating working in the first diffraction order, that was used to record spectra of the nitrogen first positive system. Spectra were acquired with a 1600×400 pixel, 16 μm pitch charge coupled device (CCD) camera (Andor Technology, Newton EMCCD) and transferred to a computer for processing. The interelectrode gap was imaged along the

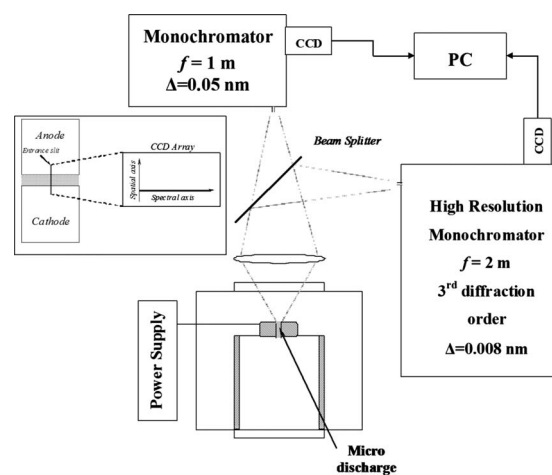


FIG. 1. Schematic diagram of the experimental apparatus. Inset at left shows the imaging of the interelectrode gap on the CCD array.

^{a)}Electronic addresses: sgbelostotskiy@gmail.com, vmdonnelly@uh.edu, and economou@uh.edu.

^{b)}Electronic mail: nader.sadeghi@ujf-grenoble.fr.

vertical length of the slits, such that one dimension of the CCD array corresponded to the emission wavelength (spectral dimension) while the other corresponded to the interelectrode gap between cathode and anode (spatial dimension), see inset in Fig. 1. 4-pixel binning was applied in the spatial dimension to improve the signal-to-noise ratio, resulting in a spatial resolution of $\sim 9 \mu\text{m}$. The spectral dispersion of the 2 m monochromator was $1.325 \cdot 10^{-2} \text{ \AA}/\text{pixel}$ at 427 nm (Ar and Ar⁺ lines) and $0.97 \cdot 10^{-2} \text{ \AA}/\text{pixel}$ at 486 nm (H β line), respectively. This resulted in a spectral resolution full width at half maximum (FWHM) of $\sim 0.065 \text{ \AA}$ and $\sim 0.05 \text{ \AA}$, respectively. The spectral resolution of the 1 m monochromator was $\sim 0.5 \text{ \AA}$ FWHM. The use of glass optics limited the spectral range to 400–700 nm. Optical filters placed in front of the entrance slit prevented superposition of different diffraction orders of the grating and also isolated the desired spectral range. The wavelength calibration of the spectrometers was checked using the clearly identified Ar⁺ lines at 4865.9 and 4867.6 \AA .

III. GAS TEMPERATURE MEASUREMENTS

For gas temperature measurements, a small amount ($<0.5\%$ by volume) of N₂ was added to the argon feed gas. Analysis of rovibrational transitions of the N₂ second positive band (C ³Π_u → B ³Π_g) is often used for gas temperature measurement because this band is relatively intense, and occurs in a noncongested region of the microdischarge spectrum.^{21,22} However, in argon plasmas, efficient and nearly-resonant energy transfer from argon metastables can populate high rotational levels of the C ³Π_u state.^{11,23} This causes a rotational distribution that is roughly bi-Maxwellian, with the tail temperature much higher than the gas temperature T_g ,^{11,23} resulting in difficulties in the determination of T_g .

On the other hand, the N₂(B ³Π_g) state lies $\sim 3\text{--}4 \text{ eV}$ below the Ar(1s₅) metastable energy level hence the highly nonresonant energy transfer from Ar(1s₅) metastables to N₂(B ³Π_g) is slow compared with electron impact excitation from the ground state N₂(X ¹Σ_g⁺). The radiative lifetime of the N₂(B ³Π_g) state ($\sim 5 \mu\text{s}$) is also significantly longer than that of the N₂(C ³Π_u) state ($\sim 40 \text{ ns}$). In high pressure discharges, the characteristic time for rotational-to-translational energy transfer between N₂(B ³Π_g) and argon is of the order of 10 ns, several orders of magnitude shorter than the radiative lifetime of the B-state.^{11,23} Therefore, the N₂(B, v) rotational distribution can be assumed to be “thermalized” with the neutral gas translational distribution ($T_{\text{rot}}=T_g$). Thus, the gas temperature can be extracted from the rotational structure of the N₂(B, v' → A, v'') emission spectrum that depends on the rotational temperature of the B-state.

The recorded spectra of the first positive band (B ³Π_g($v=4$) → A ³Σ_u⁺($v=1$) and B ³Π_g($v=5$) → A ³Σ_u⁺($v=2$)) were fit with synthetic spectra, with T_g as the fitting parameter. An example of an experimental spectrum ($P=300 \text{ Torr}$, $I=20 \text{ mA}$) is presented in Fig. 2(a). The x -axis of the grayscale plot corresponds to wavelength, while the y -axis corresponds to spatial coordinate across the interelectrode gap. The spectrum from this plot that corresponds to

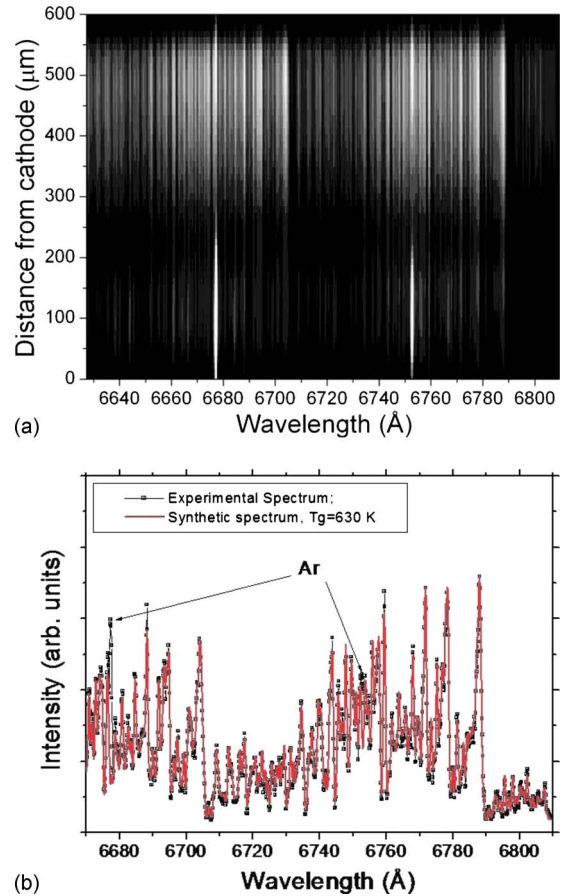


FIG. 2. (Color online) (a) CCD image of spatially resolved emission spectrum and (b) spectrum through the center of the microdischarge (points) with corresponding synthetic spectrum (line), $P=300 \text{ Torr}$ and $I=20 \text{ mA}$.

the middle of the gap, along with the best temperature fit ($T_g=630 \text{ K}$) are shown in Fig. 2(b). The arrows on the graph point to two argon emission lines [Ar($2p_1 \rightarrow 1s_4$) at $\lambda=6677.3 \text{ \AA}$ and Ar($4d_3 \rightarrow 2p_{10}$) at $\lambda=6752.8 \text{ \AA}$] that overlap with the nitrogen spectrum. The part of the spectrum with these emissions was excluded from the fit.

IV. ELECTRON DENSITY MEASUREMENTS

The spatially resolved electron density (n_e) was obtained by analyzing the Stark contribution to the broadening of the spectral profile of the H β line.^{24–26} Several broadening mechanisms influence the emission lineshape in plasmas, natural broadening (this is usually insignificant), Doppler broadening, pressure broadening, and Stark broadening.

Doppler broadening leads to a Gaussian profile, with a FWHM (Ref. 27)

$$\Delta\lambda_D = 7.16 \cdot 10^{-7} \cdot \lambda \cdot \sqrt{\frac{T}{M}} = 3.48 \cdot 10^{-4} \cdot \sqrt{T_g} \text{ (in nm)}, \quad (1)$$

where $\lambda=4861.33 \text{ \AA}$ is the central wavelength, $M=1 \text{ g/mol}$ is the atomic weight of H, and T is the temperature of H atoms, which (due to the high collision frequency) is equal to the gas temperature T_g (in K).

Pressure broadening arises from perturbation of the energy levels of the emitting atoms due to the presence of surrounding neutral species. Pressure broadening, which leads to a Lorentzian profile, is subdivided into resonance broadening (when emitters and perturbers are of the same type and either the upper or the lower state of the observed line is a resonance level), and van der Waals (*vdw*) broadening (when emitters are perturbed by neutrals of a foreign gas). In the present work, the density of H atoms was extremely low. Thus, only van der Waals broadening was considered. The FWHM of the *vdw* profile is^{30–33}

$$\Delta\lambda_P = 6.8 \times 10^{-3} \frac{P}{T_g^{0.7}} \quad (\text{in nm}), \quad (2)$$

where P is the gas pressure (Torr) and T_g is in K.

Stark broadening originates from the interaction of emitting atoms with charged particles in the plasma. The resulting lineshape can be approximated by a Lorentzian^{28–30} with FWHM

$$\Delta\lambda_S = 2.5 \times 10^{-10} \alpha(n_e, T_e) n_e^{2/3} \quad (\text{in nm}), \quad (3)$$

where n_e is electron density (cm^{-3}) and $\alpha(n_e, T_e)$ is the reduced wavelength separation, specific for the selected transition, which is generally a function of electron density n_e and electron temperature T_e . Tabulated values of $\alpha(n_e, T_e)$ for a broad range of T_e and n_e can be found elsewhere.^{28–30} However, over the parameter range of interest in this work ($T_e \approx 1–10$ eV, $n_e \approx 10^{13}–10^{14}$ cm^{-3}), the value of the reduced wavelength separation varies only slightly (<5%). Therefore, it was assumed to be constant, equal to $\alpha(n_e, T_e) = 0.077$.²⁸

The lineshape of the H_β emission profile is a superposition of all aforementioned broadening mechanisms, which results in a Voigt profile

$$f_V(\lambda) = \frac{2 \cdot \ln(2) \Delta\lambda_L}{\pi^{3/2} \Delta\lambda_G^2} \times \int_{-\infty}^{+\infty} \frac{\exp(-t^2)}{\left[2\sqrt{\ln(2)} \frac{(\lambda - \lambda_0)}{\Delta\lambda_G} - t \right]^2 + \left[\sqrt{\ln(2)} \frac{\Delta\lambda_L}{\Delta\lambda_G} \right]^2} dt, \quad (4)$$

where $\Delta\lambda_G$ and $\Delta\lambda_L$ are the widths FWHM of the Gaussian and Lorentzian components, respectively.

The parameters of the Voigt profile, Eq. (4) are as follows:

$$\Delta\lambda_G = \sqrt{\Delta\lambda_D^2 + \Delta\lambda_{GI}^2}, \quad (5)$$

$$\Delta\lambda_L = \Delta\lambda_P + \Delta\lambda_S. \quad (6)$$

The resolution of the experimental apparatus (instrumental broadening, $\Delta\lambda_{GI}$) must also be taken into account. This was deduced from the recorded linewidth of the 486.76 nm Ar^+ ($4p^2D_{3/2}^o - 3d''^2D_{3/2}$) line (shown in Fig. 3), for which Doppler, pressure, and Stark broadening are all smaller than the instrumental broadening. Fitted with a Voigt function, with $\Delta\lambda_G$ and $\Delta\lambda_L$ as fitting parameters, the experimental line-

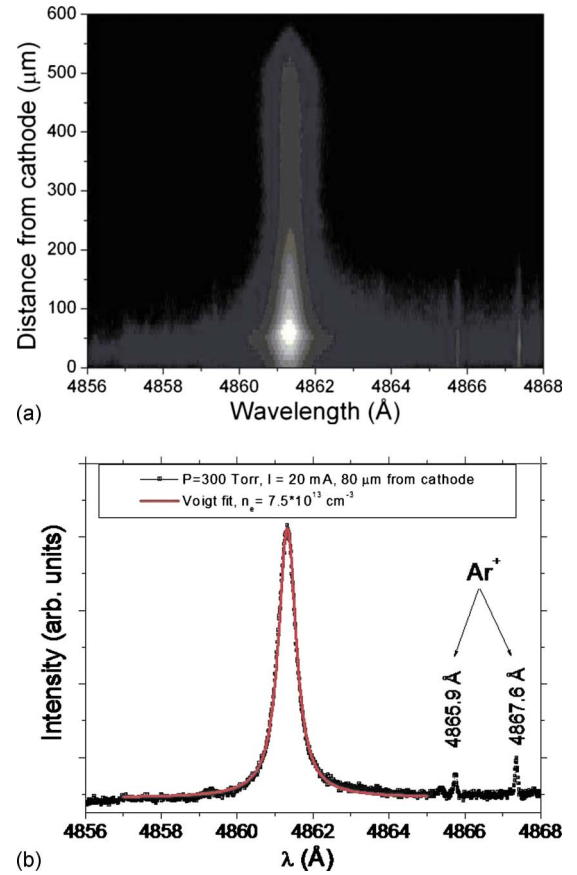


FIG. 3. (Color online) (a) CCD image of spatially resolved emission spectrum and (b) spectrum 80 μm away from the cathode (points) with the corresponding Voigt fit (line), $P=300$ Torr and $I=20$ mA.

shape of the 486.76 nm Ar^+ emission gave $\Delta\lambda_G=0.008$ nm for the Gaussian component and $\Delta\lambda_L=0.0004$ nm for the Lorentzian component. Doppler broadening was determined to be much less than 0.008 nm, permitting the assumption of a Gaussian instrumental broadening with FWHM of $\Delta\lambda_{GI}=0.008$ nm [see Eq. (5)].

A procedure to determine the gas temperature and electron density using the H_β lineshape is as follows. The measured H_β lineshape is fit to the Voigt profile of Eq. (4), whereby the values of both $\Delta\lambda_G$ and $\Delta\lambda_L$ are obtained as fitting parameters. Knowing $\Delta\lambda_G$ and the instrumental broadening $\Delta\lambda_{GI}$, Eq. (5) is used to find $\Delta\lambda_D$ and hence the gas temperature via Eq. (1). Using this gas temperature, $\Delta\lambda_P$ is determined, and Eq. (6) is used to find $\Delta\lambda_S$ and hence the electron density via Eq. (3).

In principle, this procedure should give a unique solution for both T_g and n_e . However, in the presence of noise and other distortions (e.g., gradients of n_e and T_g across the collection volume), the chi-square minimization routine, used to find the best fit, might have multiple local minima. This is especially important in the case of Voigt fits, for which $\Delta\lambda_G$ and $\Delta\lambda_L$ can each vary over a relatively broad range but give nearly the same Voigt profile. To avoid this complication, only the electron density was allowed to vary in the fit. The gas temperature was taken from the rotational spectrum of N_2 , as described in Sec. III. In this way, the Gaussian component $\Delta\lambda_G$ of the Voigt profile in Eq. (4) was fixed. The

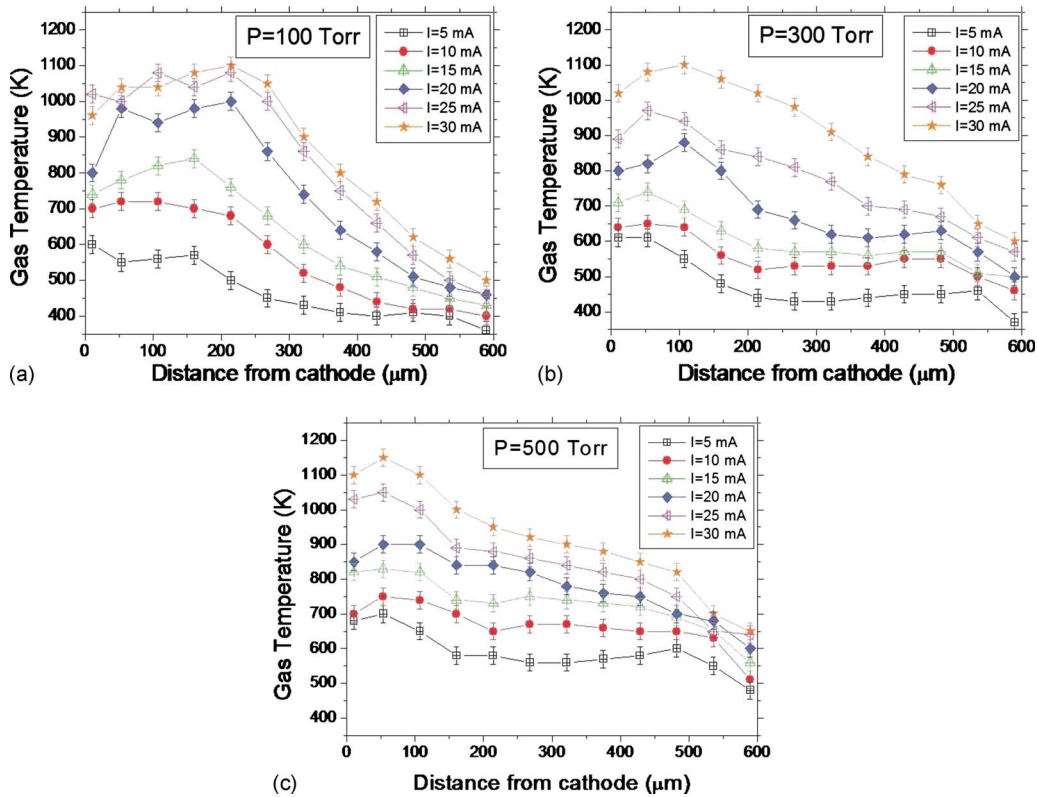


FIG. 4. (Color online) Gas temperature profiles across the interelectrode gap at different discharge currents and pressures of (a) $P=100$ Torr, (b) $P=300$ Torr, and (c) $P=500$ Torr.

measured H_{β} lineshape was then used to extract $\Delta\lambda_L$ only. Subtracting the contribution of pressure broadening, $\Delta\lambda_S$ and hence the electron density was obtained (see Eqs. (6) and (3)).

An example of spatially resolved spectrum of H_{β} emission is shown in Fig. 3(a) ($P=300$ Torr and $I=20$ mA). The lineshape at a position $80 \mu\text{m}$ away from the cathode (for which $T_g=860$ K), and the corresponding Voigt fit are shown in Fig. 3(b). Under these conditions, the electron density was calculated to be $n_e=7.5 \times 10^{13} \text{ cm}^{-3}$.

V. RESULTS AND DISCUSSION

Spatially resolved gas temperature measurements at different currents and pressures are presented in Fig. 4. The gas temperature is maximum near the cathode and decreases gradually toward the anode. As pressure increases, the spatial location of the gas temperature maximum shifts toward the cathode. These trends are consistent with the physics of dc discharges, where most of the power dissipation occurs in a narrow layer adjacent to the cathode.³¹

The results of T_g measurements obtained in the present study were compared with diode laser absorption spectroscopy data¹⁸ (see Fig. 5), at the spatial location of the peak argon metastable density ($\sim 50 \mu\text{m}$ from the cathode) and for $P=100$ Torr. Both sets of data follow the same trend with discharge current. However, the values obtained with OES are higher than those obtained by absorption spectroscopy.

This discrepancy can be explained as follows: first, the lifetime of absorbing species $\text{Ar}(1s_5)$ is longer than that for

emitting species $\text{N}_2(\text{B}^3\Pi_g)$. Therefore, $\text{Ar}(1s_5)$ metastables can diffuse farther away from the discharge, compared to $\text{N}_2(\text{B}^3\Pi_g)$ molecules, such that their line-of-sight average temperature is lower. Moreover, emission originates from the discharge (where the gas is warmer) while absorption measurements are line-integrated along the beam path, which includes regions outside the discharge. Second, absorption spectroscopy was done in pure argon microdischarges, while OES was done in microdischarges of argon with a trace of N_2 . The inset of Fig. 5 shows that, even small additions of nitrogen (0.5%), result in higher discharge voltage for the

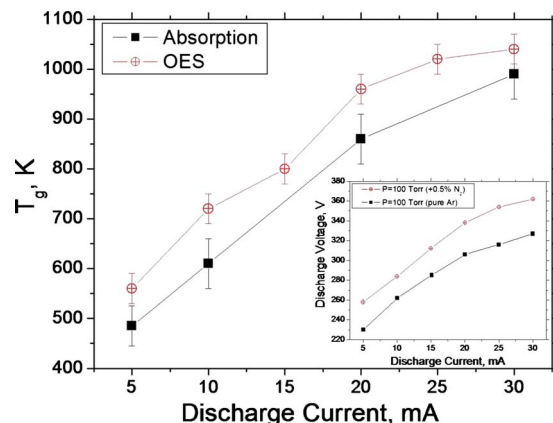


FIG. 5. (Color online) Comparison of T_g measurements obtained by laser absorption spectroscopy and OES. Inset: I - V characteristics of a pure argon microdischarge (upper curve) and of an argon microdischarge with 0.5% of N_2 (lower curve), $P=100$ Torr.

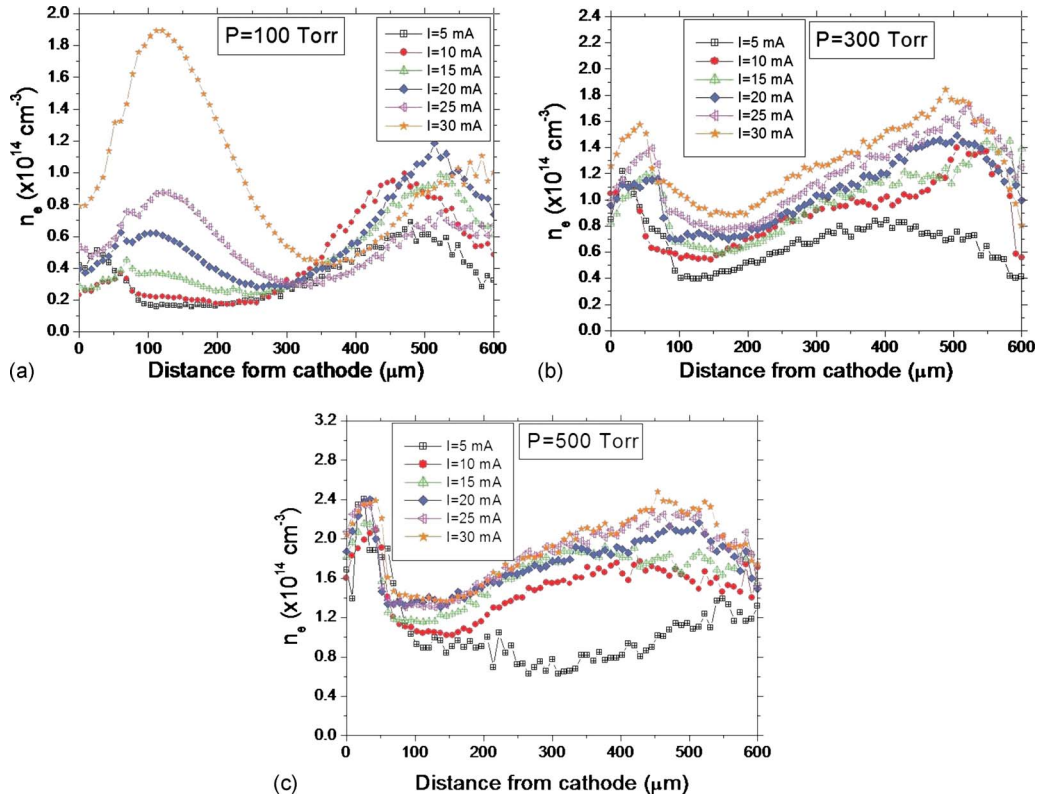


FIG. 6. (Color online) Spatial profiles of electron density at different discharge current and pressure of (a) $P=100$ Torr, (b) $P=300$ Torr, and (c) $P=500$ Torr.

same current (compared to pure argon) and, therefore, higher power deposition. This may explain the higher T_g values obtained by OES.

The spatial profiles of electron density extracted from the Stark width of the H_β lineshape are presented in Fig. 6. At fixed pressure, the plasma density increases with discharge current. The electron density has maximum in the cathode sheath edge region, followed by a minimum, and then a broad maximum on the anode side of the discharge. Such unusual behavior was not captured by a one-dimensional (1D) model of an argon microdischarge,²² or 1D models of helium microdischarges,^{10,15} including a PIC-MCC (Particle-In-Cell/Monte Carlo Collisions) simulation.¹⁵ According to the prediction of these models, the electron density should peak near the sheath edge (negative glow region) and then drop to a value that should remain approximately constant throughout the bulk plasma.

The unusual electron density profiles are not artifacts caused by errors in the gas temperature measurements that could cause an error in the Stark contribution estimates since it was found that the electron density was not very sensitive to the value of gas temperature used. Likewise, Stark splitting due to the electrostatic field cannot cause the broad peaks in electron density near the anode. Stark splitting would only impact the measurements taken inside the cathode sheath, where the electric field is relatively large. In the bulk plasma, Stark splitting is negligible due to the very low electric field in this region.

The spatial electron density distribution can be explained by the structure of the discharge. Photographs of the plasma

(see Fig. 7) reveal a bright “disk,” stretched parallel to the cathode (this corresponds to the negative glow), and a “spot” that represents a highly constricted positive column. Such structure of high pressure dc microdischarges has been reported previously.^{13,16,17}

Thermal constriction of a dc positive column, operating in a volumetric regime (i.e., electrons are mainly lost in the volume due to electron-ion recombination, as opposed to a diffusion dominated regime, where electrons are mainly lost to the chamber walls), is a well-known effect.^{31,32} Constriction

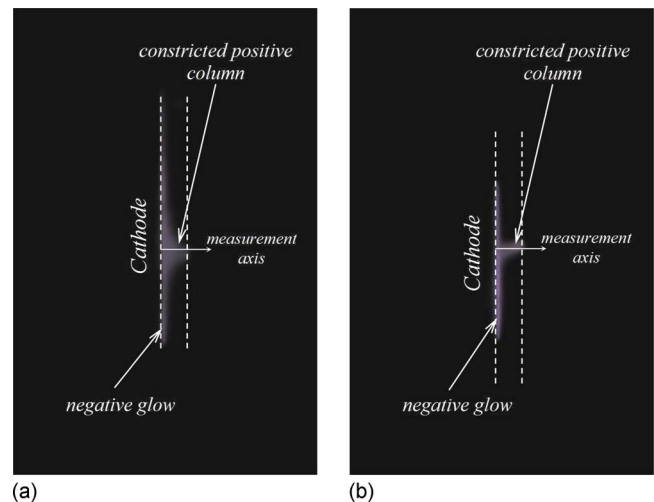


FIG. 7. (Color online) Photograph of argon dc microdischarge at $I=20$ mA, and $P=300$ Torr (left) and $P=500$ Torr (right). White dashed lines represent the approximate location of the electrodes.

tion originates from a feedback mechanism whereby a local increase (fluctuation) in gas temperature results in lower gas number density N , higher E/N , higher ionization rate and electron density, and even higher gas temperature in that region. The final result of this instability is that the discharge tends to conduct all the current through a “hot spot,” with a size determined by the distance that electrons diffuse before they recombine. This distance can be estimated as^{31,32}

$$R \approx \sqrt{\frac{6D_a}{\beta n_e}}, \quad (7)$$

where D_a is the ambipolar diffusion coefficient and β is the electron-ion volume recombination coefficient. For the main recombination reaction $\text{Ar}_2^+ + e \rightarrow \text{Ar}^* + \text{Ar}$, $\beta(\text{cm}^3/\text{s}) = 8.5 \times 10^{-7}(T_e/300)^{-2/3}$, with T_e in Kelvin.³³ For typical experimental conditions ($P \sim 500$ Torr, $T_g \sim 700$ K, $n_e \sim 10^{14} \text{ cm}^{-3}$, $T_e \sim 1$ eV), $R \sim 20 \mu\text{m}$. This estimate was made assuming that all electrons are generated in an infinitely thin channel and that their loss is mainly controlled by recombination with molecular ions Ar_2^+ . The size of the “hot spot,” is also affected by the characteristic length of the temperature gradient in and near the hot spot. Moreover, the density of Ar_2^+ ions goes down in the “hot spot” since the rate coefficient of the three body ion conversion reaction ($\text{Ar}^+ + \text{Ar} + \text{Ar} \rightarrow \text{Ar}_2^+ + \text{Ar}$) decreases with the increase in the gas temperature.³⁴ This can lead to deconstriction of the positive column, due to depletion of molecular ions (the main cause of electron loss) in the hot spot.³² In general, mathematical description of the positive column constriction is quite complicated and it is beyond the scope of the present study.

In the presence of constriction, the cross sectional area of the current flow is drastically different for the cathode sheath region (where the discharge covers most of the electrode surface) and for the positive column (where the discharge shrinks to a relatively small spot). Therefore, the current density (and therefore electron density) in the hot spot must be much higher than at the cathode sheath edge to provide continuity of current. This explains the spatial behavior of the observed electron density profiles.

Electron densities in the “valleys” (minima of the spatial n_e profiles), where the discharge is not yet constricted can be validly compared with predictions from a 1D model. These electron densities increases with both current and pressure (Fig. 8), consistent with the trends obtained with 1D models.^{10,15,22}

The n_e data obtained by OES were also compared with those obtained by LTS (Ref. 14) (see Fig. 8). Electron densities obtained by both techniques are consistent.

VI. CONCLUSIONS

Spatially resolved OES was used to measure the gas temperature and electron density profiles in a $600 \mu\text{m}$ slot-type dc microdischarge in argon with minute amounts of N_2 and H_2 present as optical tracers. The gas temperature was deduced from the rotational structure of the first positive system of N_2 ($\text{B } ^3\Pi_g(v=4) \rightarrow \text{A } ^3\Sigma_u^+(v=1)$ and $\text{B } ^3\Pi_g(v=5) \rightarrow \text{A } ^3\Sigma_u^+(v=2)$). The gas temperature increased with increasing current and pressure. The gas temperature peaked on the

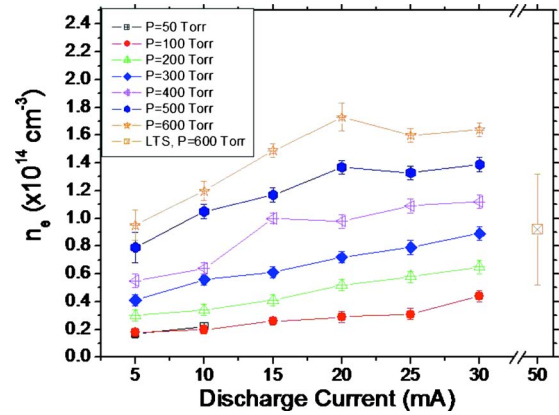


FIG. 8. (Color online) Electron density at the minimum of the spatial distribution vs discharge current at different gas pressures.

cathode side of the discharge and gradually decreased toward the anode. Such behavior is consistent with the physics of dc discharges, where most of the power dissipation occurs in a thin layer next to the cathode. The electron density was extracted from the spectral profile of the H_β line. The lineshape was fit with a Voigt function, which included Doppler, pressure, instrumental, and Stark broadening. The electron density was estimated from the contribution of Stark broadening. The electron density profiles were found to have a maximum in the cathode sheath edge region, followed by a minimum in the bulk plasma, and then another maximum some distance from the anode. This unusual spatial distribution was explained by the nonhomogeneous structure of the microdischarge, having a highly constricted positive column.

ACKNOWLEDGMENTS

The authors thank the Department of Energy (Grant No. DE-FG02-03ER54713) and the University of Houston GEAR program for financial support of this work.

- ¹K. H. Becker, K. H. Schoenbach, and J. G. Eden, *J. Phys. D* **39**, R55 (2006).
- ²M. J. Kushner, *J. Phys. D* **38**, 1633 (2005).
- ³U. Kogelschatz, *Plasma Phys. Controlled Fusion* **46**, B63 (2004).
- ⁴J. P. Boeuf, *J. Phys. D* **36**, R53 (2003).
- ⁵K. Tachibana, Y. Kishimoto, S. Kawai, T. Sakaguchi, and O. Sakai, *Plasma Phys. Controlled Fusion* **47**, A167 (2005).
- ⁶S. Hassaballa, M. Yakushiji, Y. K. Kim, K. Tomita, K. Uchino, and K. Muraoka, *IEEE Trans. Plasma Sci.* **32**, 127 (2004).
- ⁷E. Stoffels, A. J. Flikweert, W. W. Stoffels, and G. M. W. Kroesen, *Plasma Sources Sci. Technol.* **11**, 383 (2002).
- ⁸J. Hopwood, F. Iza, S. Coy, and D. B. Fenner, *J. Phys. D* **38**, 1698 (2005).
- ⁹Q. Wang, I. Koleva, V. M. Donnelly, and D. J. Economou, *J. Phys. D* **38**, 1690 (2005).
- ¹⁰Q. Wang, D. J. Economou, and V. M. Donnelly, *J. Appl. Phys.* **100**, 023301 (2006).
- ¹¹Q. Wang, F. Doll, V. M. Donnelly, D. J. Economou, N. Sadeghi, and G. F. Franz, *J. Phys. D* **40**, 4202 (2007).
- ¹²S. G. Belostotskiy, Q. Wang, V. M. Donnelly, D. J. Economou, and N. Sadeghi, *Appl. Phys. Lett.* **89**, 251503 (2006).
- ¹³S. G. Belostotskiy, V. M. Donnelly, and D. J. Economou, *Plasma Sources Sci. Technol.* **17**, 045018 (2008).
- ¹⁴S. G. Belostotskiy, R. Khandelwal, Q. Wang, V. M. Donnelly, D. J. Economou, and N. Sadeghi, *Appl. Phys. Lett.* **92**, 221507 (2008).
- ¹⁵J. Choi, F. Iza, J. K. Lee, and C. M. Ryu, *IEEE Trans. Plasma Sci.* **35**, 1274 (2007).
- ¹⁶V. I. Arkhipenko, A. A. Kirillov, Y. A. Safronau, L. V. Simonchik, and S. M. Zgironski, *Plasma Sources Sci. Technol.* **17**, 045017 (2008).

- ¹⁷D. Staack, B. Farouk, A. Gutsol, and A. Fridman, *Plasma Sources Sci. Technol.* **17**, 025013 (2008).
- ¹⁸S. G. Belostotskiy, V. M. Donnelly, D. J. Economou, and N. Sadeghi, *IEEE Trans. Plasma Sci.* **37**, 852 (2009).
- ¹⁹X. M. Zhu, W. C. Chen, and Y. K. Pu, *J. Phys. D* **41**, 6 (2008).
- ²⁰D. Mariotti, Y. Shimizu, T. Sasaki, and N. Koshizaki, *J. Appl. Phys.* **101**, 013307 (2007).
- ²¹V. M. Donnelly and M. V. Malyshev, *Appl. Phys. Lett.* **77**, 2467 (2000).
- ²²Q. Wang, Ph.D. thesis, University of Houston, 2006.
- ²³T. D. Nguyen and N. Sadeghi, *Chem. Phys.* **79**, 41 (1983).
- ²⁴J. Torres, M. J. van de Sande, J. van der Mullen, A. Gamero, and A. Sola, *Spectrochim. Acta B* **61**, 58 (2006).
- ²⁵C. O. Laux, T. G. Spence, C. H. Kruger, and R. N. Zare, *Plasma Sources Sci. Technol.* **12**, 125 (2003).
- ²⁶M. Ivkovic, S. Jovicevic, and N. Konjevic, *Spectrochim. Acta B* **59**, 591 (2004).
- ²⁷H. R. Griem, *Plasma Spectroscopy* (McGraw-Hill, New York, 1964).
- ²⁸P. Kepple and H. R. Griem, *Phys. Rev.* **173**, 317 (1968).
- ²⁹J. M. Luque, M. D. Calzada, and M. Saez, *J. Phys. B* **36**, 1573 (2003).
- ³⁰M. A. Gigoso and V. Cardenoso, *J. Phys. B* **29**, 4795 (1996).
- ³¹Y. P. Raizer, *Gas Discharge Physics* (Springer-Verlag, Berlin, 1991).
- ³²E. P. Velikhov, A. S. Kovalev, and A. T. Rakhimov, *Physical Phenomena in a Gas Discharge Plasma* (Nauka, Moscow, 1987).
- ³³F. J. Mehr and M. A. Biondi, *Phys. Rev.* **176**, 322 (1968).
- ³⁴A. Fridman and L. Kennedy, *Plasma Physics and Engineering* (Taylor & Francis, New York, 2004).